PHOTONICS Research

Dynamic nitrogen vacancy magnetometry by single-shot optical streaking microscopy

Mark A. Keppler,[1,2,*] Zachary A. Steelman,[3] Zachary N. Coker,[2] Miloš Nesládek,[4,5,6] Philip R. Hemmer,[7] Vladislav V. Yakovlev,[1,9] and Joel N. Bixler[8]

[1]Department of Biomedical Engineering, Texas A&M University, College Station, Texas 77843, USA
[2]SAIC, JBSA Fort Sam Houston, Texas 78234, USA
[3]National Research Council Research Associateship Program, Washington, DC 20001, USA
[4]IMOMEC Division, IMEC, B-3590 Diepenbeek, Belgium
[5]Institute for Materials Research (IMO), Hasselt University, B-3590 Diepenbeek, Belgium
[6]Czech Technical University in Prague, 27201 Kladno, Czech Republic
[7]Department of Electrical and Computer Engineering, Texas A&M University, College Station, Texas 77843, USA
[8]Bioeffects Division, Airman System Directorate, Air Force Research Laboratory, JBSA Fort Sam Houston, Texas 78234, USA
[9]e-mail: yakovlev@tamu.edu
*Corresponding author: keppler.mark@gmail.com

Received 7 February 2022; revised 14 June 2022; accepted 15 June 2022; posted 20 July 2022 (Doc. ID 455634); published 26 August 2022

Nitrogen vacancy diamonds have emerged as sensitive solid-state magnetic field sensors capable of producing diffraction limited and sub-diffraction field images. Here, for the first time, to our knowledge, we extend those measurements to high-speed imaging, which can be readily applied to analyze currents and magnetic field dynamics in circuits on a microscopic scale. To overcome detector acquisition rate limitations, we designed an optical streaking nitrogen vacancy microscope to acquire two-dimensional spatiotemporal kymograms. We demonstrate magnetic field wave imaging with micro-scale spatial extent and ~400 μs temporal resolution. In validating this system, we detected magnetic fields down to 10 μT for 40 Hz magnetic fields using single-shot imaging and captured the spatial transit of an electromagnetic needle at streak rates as high as 110 μm/ms. This design has the capability to be readily extended to full 3D video acquisition by utilizing compressed sensing techniques and a potential for further improvement of spatial resolution, acquisition speed, and sensitivity. The device opens opportunities to many potential applications where transient magnetic events can be isolated to a single spatial axis, such as acquiring spatially propagating action potentials for brain imaging and remotely interrogating integrated circuits.

https://doi.org/10.1364/PRJ.455634

1. INTRODUCTION

Nitrogen vacancies (NVs) are fluorescent point defects composed of a substitutional nitrogen located adjacent to a vacancy within a diamond carbon lattice that can optically measure small-scale magnetic field fluctuations through the Zeeman effect [1]. NV implanted diamonds have emerged as effective solid-state magnetic field sensors with applications spanning physics, biomedical science, and geology [2–6]. Due to the atomic scale of each NV color center, ensembles of NVs as thin layers embedded in chemical vapor deposition (CVD) diamonds can produce detailed diffraction limited and sub-diffraction images of spin projected magnetic fields [7,8]. The rigid tetrahedral diamond geometry results in NVs having one primary and three secondary sensing axes, each capable of measuring projected components of the local field potential [9]. As such, NV centers can accurately and repeatably detect field magnitude and orientation.

NV utility in biomedical applications has been demonstrated through detection of magnetic fields during stimulated neural signaling in living organisms, mapping of magnetic field strength and orientation in magnetotactic bacteria, tagging *in vivo* functional groups with NV fluorescent probes, and real-time cellular temperature measurement, both *in vitro* and in living organisms [10–14]. This proliferation of biomedical applications is enabled by the inherent biocompatibility of diamond, along with demonstrated long spin and coherence lifetimes and magnetic field sensitivities of ~15 $\mathrm{pT}/\sqrt{\mathrm{Hz}}$ at room temperature [10].

Magnetic field sensing dynamics can be understood from a simplified NV model that assumes four primary electronic states populated by electrons with magnetic spin-states $m_s = \{0, +1, -1\}$ [15]. Under 532 nm illumination, NVs undergo a spin-preserving radiative transition from an $^3A_2$ orbital-singlet and spin-triplet ground state to an excited orbital-doublet and

spin-triplet ^{3}E emitting broadband fluorescence with a wavelength range of 600–800 nm. A secondary spin-polarizing non-radiative pathway from ^{3}E to $^3A_2$ consists of two metastable singlet states $^1A_1$ and ^{1}E, which preferentially converts electrons with $m_s = \pm 1$ to $m_s = 0$. By applying radio frequency (RF) energy around 2.87 GHz, electrons with $m_s = 0$ can be externally converted to $m_s = \pm 1$, verified by a decrease in fluorescence intensity, which localizes the spin states. In the presence of a magnetic field B, Zeeman splitting of the degenerate $m_s = \pm 1$ electrons causes the RF necessary to localize each spin state to be offset from 2.87 GHz by $\pm\gamma B$, where γ is the gyromagnetic ratio of the NV center. Magnetic field intensity can therefore be related to the RF dependent variations in fluorescence intensity, a process known as optically detectable magnetic resonance (ODMR) [16].

While there is much interest in NV sensors for magnetic field imaging, transitioning to high-speed micro-scale video recording has been slow. Trade-offs among camera cost, spatial resolution, and frame rate place strict constraints on research progress [17]. While inexpensive high-speed cameras do exist, they typically have low bit-depth and dynamic range. High read-out rates also increase read noise, which has a pronounced effect on low photon count imaging such as high-speed quantum sensing. Full resolution acquisition rates for modern scientific-grade complementary metal–oxide semi-conductor (sCMOS) cameras typically do not exceed 30–100 frames per second (fps) [18]. The frame rate can be increased by restricting the region of interest (ROI); however, for the particular sCMOS used in experiments, the smallest ROI (2048 × 40) corresponds to a frame rate of 850 fps (or 1.2 ms frame-to-frame interval). Many bioelectric cellular processes occur of the order of a few milliseconds, making sub-millisecond magnetometry with micro-scale spatial resolution highly desirable [19,20]. Sub-ms magnetometry could also find applications in analyzing fast integrated circuits, which has been mostly limited to temporally integrated information [7,21].

To overcome detector acquisition rate limitations, we designed an optical streaking NV microscope that uses a galvo-scanner to generate two-dimensional (2D) spatiotemporal kymograms. Optical streaking generates kymograms by the spatial translation of an image focused on the focal plane array of a camera using a galvo-mirror. While optical systems can capture full 2D spatial images, spatial translation can result in overlap between adjacent time steps. As such, the spatial extent of the images is restricted along the streak axis using a spatial mask. This procedure trades spatial information in one dimension for a six-fold increase in temporal resolution without significantly modifying standard laboratory microscopes. The design includes a software toggle to switch between full frame imaging and streak imaging to avoid limiting our general-purpose microscope to optical streaking. Here we demonstrate single-snapshot kymographic imaging of highly dynamic and spatially varying micro-scale magnetic fields by combining optical streaking with continuous-wave ODMR (cw-ODMR). We demonstrate magnetic field imaging with sub-millisecond resolution by capturing the spatial transit of a micro-scale electromagnet moving laterally across the NV sensor, while simultaneously modulating the electromagnet current in time.

2. MATERIALS AND METHODS

A. Optical Streaking Concept

Optical streaking involves the direct encoding of discrete time intervals by translation to spatial positions on a camera sensor. The optical streaking microscope can be understood as a linear operation that transforms an intensity map at the sample plane of the imaging system into a streaked digital image [22].

As seen in Fig. 1, the intensity map at the microscope's sample plane is imaged to a narrow spatial aperture placed at the primary image plane, which reduces the extent of the image along a single spatial dimension. The reduced image is linearly separated by optical streaking via a galvo-scanning mirror to encode time as a function of spatial position, then reimaged

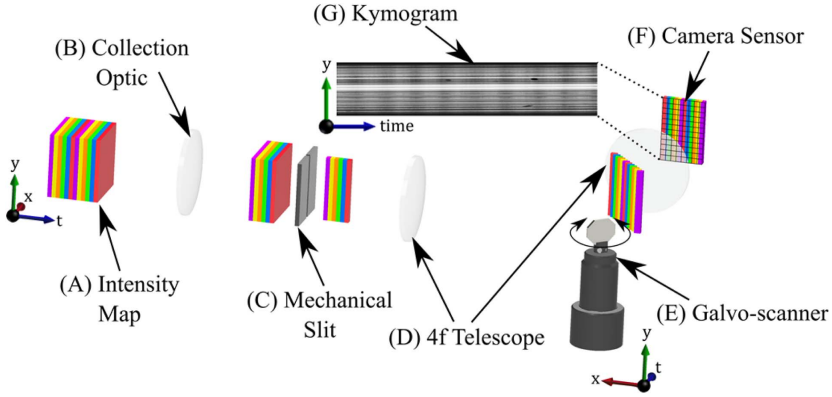

Fig. 1. Intensity map (A) at the sample plane of a collection optic (B) is imaged to a narrow spatial mask (C) at the primary image plane. Individual colors indicate time steps. The mask constrains a single spatial dimension before the reduced intensity map is re-imaged to a detector by a 4f telescope (D). A galvo-scanner (E) at the telescope's Fourier plane provides a constant velocity streaking operator, separating temporal information as a function of spatial position. The reduced and streaked scene is then imaged to the camera sensor (F) by the second $4f$ telescope lens where the information is encoded and digitized as a kymogram (G). Spatial masking minimizes the overlap between adjacent time steps on the detector after optical streaking. An example of an optically streaked sinusoidal magnetic field is displayed with corresponding $y - t$ spatiotemporal coordinates. While results demonstrated below focus on microscopy, this general concept can be readily adapted to many imaging systems.

to the camera sensor. Spatial reduction, accomplished by the aperture, minimizes the amount of overlap between temporally unique data at the detector. The camera sensor encodes the streaked data from the entire temporal exposure window into a single pixel-space image.

B. Optical System

An NV optical streaking magnetometer was designed around a laboratory-built widefield fluorescence microscope. A simplified CAD model of this system is provided in Fig. 2. Continuous optical excitation at 532 nm was provided by a frequency-doubled diode pumped solid-state Nd:YVO_4 laser (Compass 415M, Coherent) with a Gaussian beam profile providing approximately 3.7 kW cm^{-2} at the sample plane. A 380 μm diameter spot ($1/e^2$) was illuminated at the NV diamond sensor by focusing a collimated beam to the back focal plane of a 10× 0.28 NA long working distance objective (OBJ) (10× M Plan APO, Mitotuyo) with a 250 mm plano–convex lens (L1). Fluorescence was separated from the source illumination with a 540 nm long-pass dichroic mirror (DM) (LP03-532RU-25, Semrock) and a subsequent 650 nm long-pass filter (LPF) (FEL0650, Thorlabs). Free-space projection of the primary image plane formed by an apochromatic tube lens with 200 mm focal length (L2) to an sCMOS detector (Dhyana 95 v1, Tucsen) was accomplished using a 1.5× relay telescope consisting of a 100 mm (L3) and 150 mm (L4) achromat with a galvo-scanning mirror (GS) (GVS002, Thorlabs) located at the telescope's Fourier plane. A mechanical slit (MS) was used to balance temporal resolution and optical throughput. All images were acquired with the sCMOS high dynamic range (HDR) mode and 2 × 2 pixel binning.

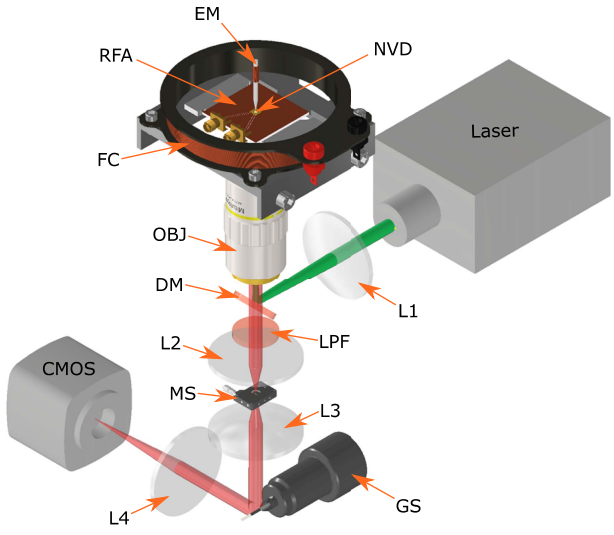

Fig. 2. NV optical streaking magnetometer designed around a widefield fluorescence microscope is depicted. A 532 nm laser (green) was focused to the back focal plane of a long working distance objective (OBJ) by a plano–convex lens (L1). NV fluorescence (red) was separated from the source by a dichroic mirror (DM) and a long-pass filter LPF. The NV diamond sensor (NVD) was mounted on a printed circuit board with a co-planar microstrip RF antenna loop (RFA). An optical window at the center of the RF antenna allowed for illumination and fluorescence collection. A field coil (FC) was centered on the NV sensor such that spatially uniform magnetic fields could be generated. Spatially varying magnetic fields were generated with a permalloy electromagnetic needle (EM) wrapped with a coil fixed to a rotational mount. To reduce the amount of overlap between adjacent time steps, a mechanical slit (MS) was positioned at the primary image plane formed by the tube lens (L2). Optical streaking was achieved with a galvo-scanner (GS) positioned at the Fourier plane of a 4f telescope (L3 and L4) coupling the primary image plane to the detector (CMOS). Cylindrical beams and conic focal points are depicted to differentiate between infinity space and image planes, respectively. Components were not drawn to scale to assist with visibility of the optical path.

C. Magnetic Field Detection

Magnetic field detection was achieved by cw-ODMR [23,24]. A continuous 2.874 GHz + 7 dBm RF sine wave was generated by a SynthNV PRO (Windfreak, LLC) and amplified by +45 dB (ZHL-16W-43+, Mini-Circuits). A 50 Ω coplanar microstrip antenna etched into a two-layer printed circuit board (PCB) was used to couple the RF signal to a 5 mm × 5 mm × 1 mm NV diamond sensor. The sample consisted of an epitaxial CVD layer grown on (100) high-pressure high-temperature (HPHT) low N concentration diamond substrate (<50 ppb N) from New Diamond Technology (Russia). The growth conditions were as follows: pressure 130 Torr, microwave power 1200 W, CH_4 concentration in H_2 carrier gas 3.5% (7 sccm), with total flow of 200 sccm. The sample was doped by nitrogen from a N_2 (1%)–H_2 gas mixture and co-doped with phosphorus from PH_3 (1000 ppm)–H_2 gas mixture sources. The N_2–H_2 mixture flow was adjusted to the CH_4 flow (7 sccm) and PH_3–H_2 mixture flow was 10 times higher to compensate for the lower P incorporation ratio, targeting ∼5 ppm concentration of N and P in the grown layer. The growth substrate temperature was 900°C and the final thickness of the layer was 8 μm, using approximately 1 μm/h growth rate. Neither post irradiation nor annealing was performed on the sensor. Imaging was accommodated by routing the microstrip line around a 2 mm window drilled through the PCB. The thin NV layer was positioned distal to the RF antenna and illuminated through the back face of the diamond. Continuous monitoring of the RF control signal was facilitated by a USB spectrum analyzer (SA0314, RF Instruments).

D. Hardware and Timing Control

Figure 3 shows the simplified hardware and connection diagram for the optical streaking system. System timing was synchronized by a rising edge delivered to an externally triggered digital pulse/delay generator (PGEN) (DG535, Stanford Research Systems) via a data acquisition (DAQ) card (National Instruments) controlled by custom LabVIEW software. The timing diagram in Fig. 3 shows the pulse control protocol for a single kymograph acquisition. Each waveform in the timing diagram is vertically offset and referenced to a common voltage V_{ref} for improved readability. The red PGEN timing signal shows the TTL voltage sent to trigger the galvo-scanner voltage ramp and magnetic modulation at the function generator (DG1022Z, Rigol). Both the blue magnetic sinusoidal field and green galvo-scanner ramp voltages were set to burst mode on the function generator. A second pulse beginning at t_H and ending at t_L was calibrated to coincide with the galvo-scanner ramp voltages V_H and V_L, such that an image of the narrowed slit intersected the left and right sensor edges at each voltage,

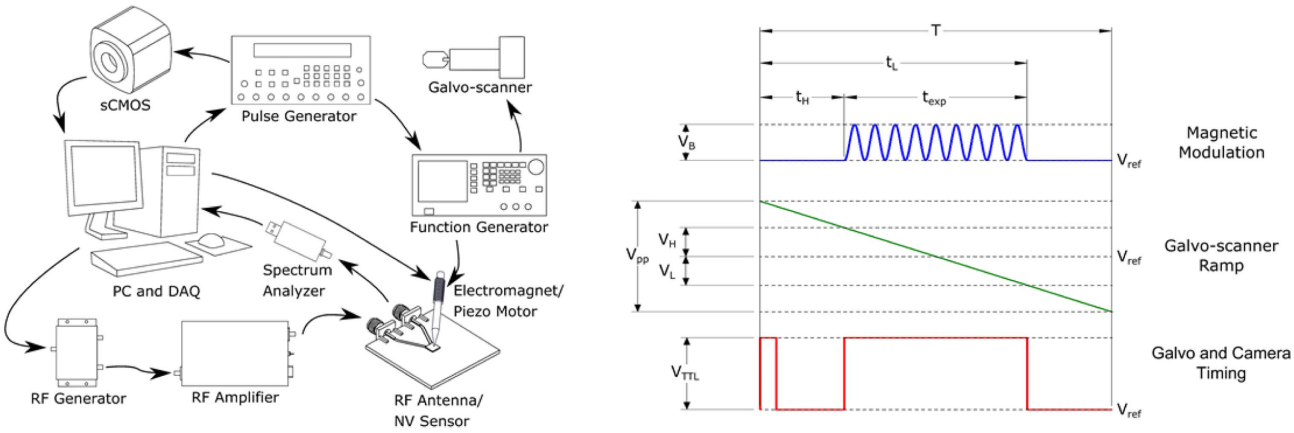

Fig. 3. (Left) Simplified block diagram demonstrating the streak control system. A PC data acquisition card provided the TTL signal to start the PGEN and serial communications with the RF generator. System timing was provided by a digital PGEN through TTL signals sent to trigger the camera and a function generator. Magnetic field and ramp voltages were output from the function generator to the magnetic field coil and galvo-scanner, respectively. Continuous RF was amplified before being coupled to the NV diamond by a coplanar microstrip antenna loop. (Right) The optical streak system timing diagram is shown for a single acquisition period T. Each waveform in the timing diagram is offset and referenced to a common voltage V_{ref} for improved readability. (Red) "Galvo and Camera Timing" TTL pulse sequence output by the digital pulse/delay generator to initiate the galvo-mirror ramp and trigger the camera. The initial pulse starts the "Galvo-scanner Ramp" voltage (green) at the function generator. The width of the second pulse t_{exp} sets the acquisition time of the streak image. (Blue) Magnetic field control voltage output by the function generator triggered by the second TTL pulse. The magnetic field output is triggered by the rising edge of the pulse sent to trigger the camera.

respectively. The width of the second timing pulse controlled the camera exposure duration and length of the magnetic field burst interval, t_{exp}. The time T represents half of the period of a triangle waveform sent to drive the galvo controller. The second half of the period returns the galvo mirror to the starting position prior to each acquisition. The magnetic modulation was sent to drive both the electromagnetic needle coil and the larger coil used for sensitivity analysis.

E. Electromagnet Fabrication

Electromagnets were manufactured by acid etching 1 mm Permalloy 80 wire (KND1564, ESPI Metals) in an 8:7:5 ratio by volume solution of phosphoric acid, sulfuric acid, and DI water, respectively [25]. The Permalloy 80 consisted of 80% nickel, 5% molybdenum, and 15% iron. Stock solutions of 85% (wt/wt) phosphoric acid and 95% (wt/wt) sulfuric acid were mixed with DI water and transferred to a 10 mL glass vial. Etching was accomplished by electrolysis with the permalloy wire as the cathode and a filed steel nail as the anode. Sections cut from 200 μL Eppendorf pipette tips were used to protect permalloy surfaces not being etched as outlined in Ref. [25]. Voltage was applied, starting with 6 V DC for coarse etching, and reduced to 3 V DC once the exposed wire had visibly narrowed. The acid solution was reused to produce several needles; however, etching time was adjusted to account for increasing salt concentration. The coil was then wound with 44 American wire gauge (AWG) copper magnet wire until the coil was approximately 18 mm in length and had a resistance of 50 Ω. The tip size was verified by comparison to a standard 1951 USAF resolution target via a bright-field microscope.

F. Minimum Detectable Field Analysis

The minimum detectable magnetic field sensitivity was evaluated by applying continuous illumination and RF coupling to the NV diamond. The sensor was centered both axially and radially on a large 9 cm diameter field coil designed to approximate uniform magnetic field intensity across the field of view. Streak images were acquired with a 225 ms exposure duration at 110 μm/ms (5 pix/ms) streak rate at the camera sensor verified with an optical chopper wheel. A mechanical slit at the primary image plane was adjusted to provide an image ∼10 μm wide at the camera sensor to balance optical throughput and temporal resolution. ODMR plots were acquired by sweeping the RF from 2830 to 2910 MHz in 0.5 MHz steps and then calculating the average intensity across the resulting streak at each frequency with no applied magnetic field modulation. A static bias magnetic field was applied with a neodymium magnet positioned near the NV diamond surface to induce sufficient spin-state separation resulting in two distinct Lorentzian peaks. A 40 Hz sinusoidal voltage was applied to the field coil to produce roughly 50 μT root mean square (RMS). The field intensity was determined by an on-axis magnetic field calculation using the coil's measurements [26]. An LCR meter (DE-5000, DER EE) was used to verify that the coil resistance and inductance met design specifications. With the sinusoidal field applied, the RF was again swept from 2830 to 2910 MHz in 0.5 MHz steps to determine the frequencies with optimal magnetic field response. Prior to each signal measurement, the sinusoidal field was turned off and a background streak was acquired without an applied field. We calculated the RMS field intensity I_{RMS} as the standard deviation of the signal acquired by the camera to compensate for the positive DC signal offset. The signal and background streak image replicates were averaged separately, averaged background streak images were subtracted from the averaged signal streak images, spatial components (image rows) of the difference streak image were averaged to produce intensity profile versus time plots, a bandpass

filter was applied with 20 and 60 Hz corner frequencies at a sampling rate equal to the streak rate, and the RMS of each resulting filtered profile plot was calculated with Eq. (1):

$$I_{\mathrm{RMS}} = \sqrt{\frac{1}{N}\sum_{n=1}^{N} |I_t - \bar{I}_t|^2}. \quad (1)$$

In Eq. (1), I_t is the intensity at each discrete time interval, and N is the number of time intervals across the streak profile. The imaged positive offset from the sinusoidal signal was removed by subtracting the average intensity $\bar{I}_t$. The RF generator was set to 2874 MHz, which was found to coincide with the maximum RMS field intensity. RMS magnetic field measurements were acquired from 0 to 50 μT by adjusting the voltage across the field coil.

G. Optical Streaking NV Magnetometry

To demonstrate acquisition of both spatial and sub-millisecond temporal information within a single snapshot, an optically streaked sinusoidal magnetic field was measured from a spatially translating permalloy electromagnetic needle tip. The needle was fixed to a piezo-electric rotation mount such that the needle axis was orthogonal to the plane of the diamond. A serial trigger sent to the rotation mount translated the needle along the spatial axis of the NV diamond at a rate of ∼1 μm/ms, while a 40 Hz sinusoidal voltage was applied to the electromagnet control coil wrapped around the needle. Kymograms were acquired at a streak rate of 5 pixel/ms with a 225 ms exposure verified with an optical chopper wheel. A mechanical slit was placed at the primary image plane and closed to produce an ∼10 μm wide field of view to balance temporal resolution and optical throughput. Optically detected magnetic resonance was detected under continuous 532 nm illumination and continuous RF coupling at 2874 MHz.

3. RESULTS AND DISCUSSION

A. Magnetic Field Optimization and Sensitivity Analysis

An optimization and magnetic sensitivity analysis was performed to demonstrate the NV sensor's ability to detect sinusoidal magnetic field modulations during optical streaking [27]. A neodymium bias magnet was positioned near the sensor to ensure that the weak sinusoidal fields would overcome the 8–9 MHz of splitting exhibited by the NV sensor under zero-field conditions. A small amount of splitting in the $m_s = \pm 1$ spin states is common under low to zero-field conditions, attributable to lattice strain [28,29], paramagnetic impurities, charge dynamics, and NV–NV dipolar interactions within the local environment surrounding NV spin centers [30].

Streak images were obtained while scanning the RF from 2830 to 2910 MHz with a slit width of ∼10 μm. An ODMR plot of the average intensity across each streak as a function of RF can be seen in Fig. 4A. Results indicate the bias magnet produced roughly 17 MHz of Zeeman splitting between peaks, which is sufficient to measure sinusoidal fields less than 50 μT RMS (Fig. 4D). The nearly 10% fluorescence contrast can be attributed to a non-linear gain introduced by the sCMOS in HDR mode. The ODMR was re-acquired using the sCMOS low gain mode, which demonstrates that the actual contrast of the sample was less than 4%. Operating in low gain mode also resulted in a larger measurement error that we attribute to the decrease in slope of the ODMR curve. Since the optical streaking mechanism is independent of magnetometry, future improvements in magnetometry do not detract from the increased temporal resolution of the streaking method. The additional contrast provided by HDR mode does increase SNR; therefore, it may be useful to correct for non-linearity and continue to use the technique, with the caveat that any quantitative measurements must be validated against well-characterized field sources to ensure accuracy.

Streak magnetic sensitivity was then optimized by performing a subsequent frequency sweep under an applied 40 Hz spatially uniform sinusoidal field. Profile plots of the normalized average intensity across each streak image were calculated (Fig. 4B) for each RF.

Figure 4C shows four RMS maxima that roughly coincide with the steepest tangent lines to the ODMR plot. The RMS amplitude of the intensity profiles at each RF was calculated using Eq. (1). It is to be expected that small changes in the Zeeman splitting bandwidth caused by magnetic field modulation would produce the maximum change in fluorescence intensity at these points. The vertical dashed red line at 2874 MHz indicates the RF with the best sensitivity to sinusoidal field oscillations. While it is possible, and quite common, to determine the optimal RF from the derivative of the ODMR curve in Fig. 4A, determining the optimal sensitivity from the RMS intensity provides validation for the optical streaking method [31].

The sinusoidal magnetic field profile in Fig. 4B and all field measurements that follow were acquired at 2874 MHz. A linear response was observed for magnetic field intensities down to approximately 10 μT (Fig. 4D), demonstrating an approximately linear trend in RMS intensity with respect to decreasing magnetic field strength over the observed range.

B. Optical Streaking NV Magnetometry

Our system was designed to capture sub-millisecond diffraction limited magnetic field variations of spatially propagating phenomena. As a validation, a chemically sharpened electromagnetized permalloy needle tip was mechanically translated near the surface of the NV diamond during image acquisition.

Figure 5A shows a 50% transparent image of a standard 1951 USAF resolution test target registered with an image of the needle taken with a bright-field microscope immediately after streak acquisition. The needle tip was placed adjacent to the horizontal bars of group 3 element 3 with a known width of 49.6 ± 0.5 μm, such that the diameter of the tip can be observed as ∼50 μm.

The magnetic field profile from the needle placed adjacent to the diamond (Fig. 5B) was acquired with the slit open, needle stationary, and 50 μT DC applied field. An image of the background intensity map without an applied field to the needle was subtracted to resolve the magnetic profile of the needle and the surrounding solenoidal field. Regions of positive contrast resulting from fields produced by the needle are found close to the needle tip, while negative contrast regions distant from the needle are due to the opposite orientation of the

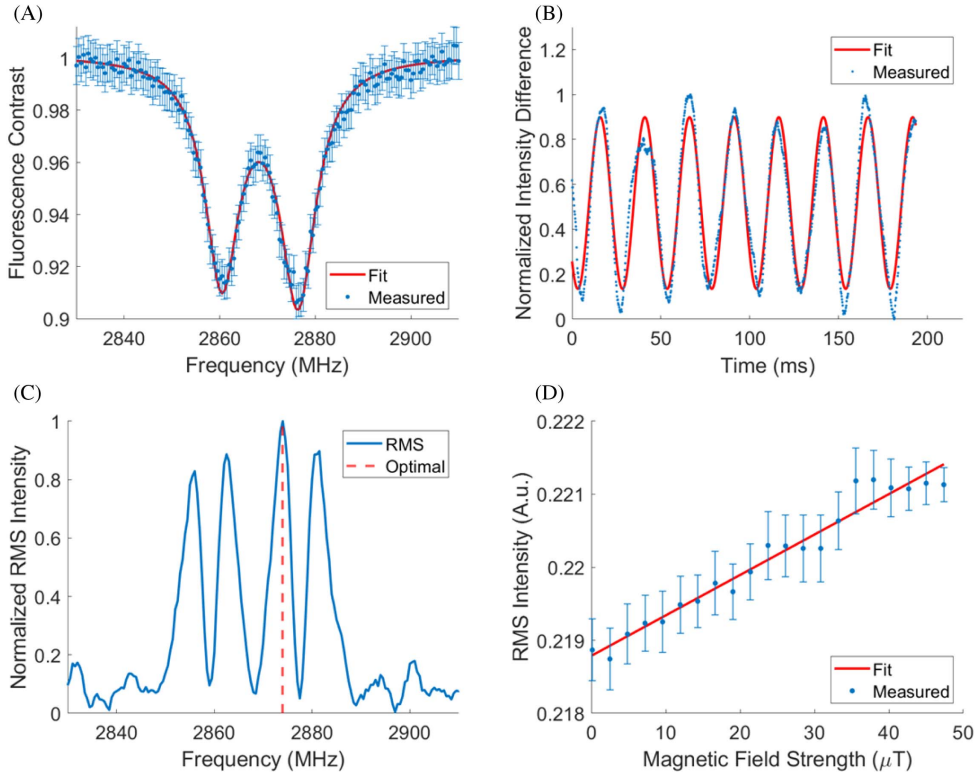

Fig. 4. Optimization and magnetic sensitivity analysis to demonstrate proper NV function as a magnetometer during optical streaking. (A) ODMR plot of the average intensity across each streak as a function of RF from 2830 to 2910 MHz acquired with an ∼10 μm slit width ($N = 200$ averages). Zeeman peak splitting of 17 MHz can be observed corresponding to the DC bias field from a neodymium magnet. (B) Profile plot of the average fluorescence contrast across a streak image calculated at 2874 MHz ($N = 200$ averages), indicated by the dashed vertical red line in (C). (C) Optical streaking under a spatially uniform 40 Hz magnetic field ($N = 1$) shows optimal RMS intensity roughly at the steepest tangents to the ODMR curve. The RMS amplitude of the intensity profiles at each RF was calculated using Eq. (1). (D) Average RMS intensity acquired from kymograms ($N = 100$ averages) while decreasing the coil driving voltage shows linear field sensitivity down to around 10 μT. Error bars represent standard deviation from the mean.

solenoidal field lines. The sharp drop-off in the magnetic field appears to correlate well with the ∼50 μm diameter from the test target measurement.

Background-subtracted lateral motion of the electromagnet at ∼1 μm/ms can be seen in Fig. 5C ($N = 10$ averages) with a 40 Hz sinusoidal magnetic field applied. The magnetic field was produced by current directed through a coil wrapped around the shaft of the needle ∼2 cm from the needle tip. Background images were produced with identical streak parameters and no applied field. At the 5 pixel/ms streak rates, each pixel spanned a minimum of 200 μs. Since the smallest temporal feature must span at least two pixels to be resolved, based on the Nyquist sampling criterion, the maximum temporal resolution the system achieved was 400 μs following the Nyquist criterion. The vertical striations in Fig. 5C above and below the bright needle tip can be attributed to the sinusoidal field from the coil and needle field interacting with the NV centers. In Fig. 5B, the needle field is seen as a positive change in the fluorescence contrast, while the solenoidal field yields a negative contrast distant from the needle, likely due to the opposite orientation of the field lines.

A profile plot of the electromagnet path seen in Fig. 5D was created by plotting the intensities along a Manhattan trajectory represented by dashed horizontal yellow lines where the horizontal rows cross through the centroid of each bright region in Fig. 5C. A bandpass filter with 20 and 60 Hz corner frequencies was used with a sampling rate equal to the streak rate to reduce high-frequency noise components. The increase in fluorescence contrast resulting from the needle field is roughly 5%, while the solenoidal field has a negative 3% contrast. The total contrast falls within the ∼10% maximum possible contrast seen in Fig. 4. The beam profile used was approximately Gaussian as verified by the fluorescence intensity profile on the NV sensor. Spatial fluorescence variations could be observed that are likely attributable to beam hot spots and differences in NV density. These variations result in pumping efficiency changes along the image of the slit. The absolute fluorescence contrast found while performing a frequency sweep was ∼10% near the center of the laser spot but reduces by as much as 10% (∼9% absolute contrast) near the top and bottom of the slit. Despite this decrease in absolute fluorescence contrast, the fluorescence contrast difference (∼5% difference) generated by needle magnetic field fluctuations seen in Figs. 5C and 5D does not appear to show a significant change from the top left corner of the streak to the bottom right corner owing to the pixel-wise normalization of the signal streak image to the background streak image.

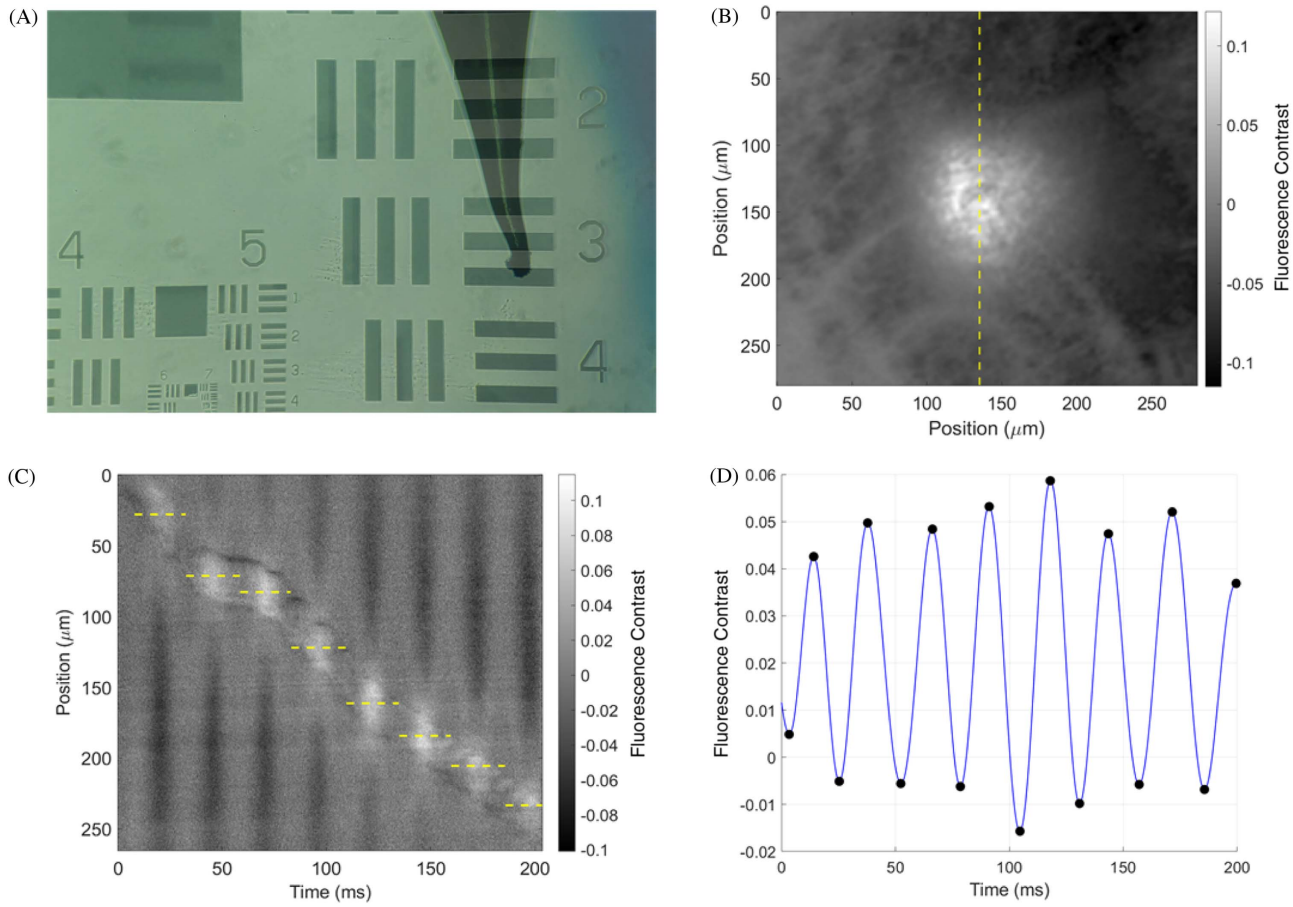

Fig. 5. Demonstration of magnetic field intensity plots obtained by optically streaking an electromagnetic needle moving laterally across the NV diamond sensor and validation of needle size. (A) A 50% transparent image of a 1951 USAF resolution test target was registered with an image of the needle such that the tip was adjacent to the horizontal bars of group 3 element 3 with a known width of 49.61 μm. (B) Magnetic field profile near the electromagnet imaged with the slit open and the needle stationary quantified by the change in fluorescence contrast from the background streak. A vertical dashed yellow line indicates the slice of the image captured by the narrow slit. The magnetic field intensity drops off sharply as the sharpened tip of the electromagnet recedes from the NV sensor that supports the ∼50 μm diameter measured in (A). A kymogram in (C) shows 200 ms of a 5 pixel/ms streak rate acquisition of the electromagnet moving at ∼1 μm/ms from top to bottom. The kymogram displays spatial information about the needle transit across the vertical axis and temporal information along the horizontal axis. Intensities represent relative changes in the fluorescence contrast as the needle is modulated with a sinusoidal field. Vertical striations in (C) are produced by a 40 Hz field modulation. (D) Bandpass filtered profile plot following the electromagnet centroid trajectory, represented by the yellow dashed lines in (C), demonstrating a measured frequency of 39.7 ± 1.2 Hz taken as the reciprocal of the average time between wave peaks and troughs.

The SNR across the slit also decreases by a factor of two near the edges of the slit. Increasing the beam power or providing flat illumination can compensate for the lack of pump efficiency; however, increased power broadening could also decrease sensitivity [32]. A heat sink may also be required to compensate for increased thermal noise [20]. A frequency of 39.7 ± 1.2 Hz was calculated using the average interval between the profile plot peaks and troughs as determined by a peak finding algorithm (MATLAB).

C. Future Direction and Applications

We have demonstrated optical streaking magnetometry with a maximum temporal resolution of ∼400 μs, which could be doubled by imaging at a reduced SNR without 2 × 2 pixel binning. The minimum detectable magnetic field strength of 10 μT may be improved by using a stronger bias field to separate the four tetrahedral NV orientations, thereby eliminating ambiguous fluorescence modulations from superposition of spin states and making the Lorentzian transitions sharper. Since the streaking mechanism is independent of the camera, higher sensitivity could be achieved by upgrading to a camera with improved read noise, thermoelectric cooling, and electron-multiplying (EM) gain. Optical streaking will provide an increase in the temporal resolution; however, high magnetic field sensitivity will be limited by the detector quantum efficiency, fill factor, and full well capacity [17]. As is, the maximum achievable SNR is also limited by the presence of background signal from different time points as the image of the slit streaks across the detector. Detector cost will still necessarily scale with the sensitivity requirements of the project, as there are few detectors that can achieve high sensitivity and low noise at kHz to MHz frame rates.

The maximum spatial extent for the optical arrangement in Fig. 2 is limited to 120 μm owing to the choice of optics and

use of small (5 mm) two-axis galvo-scanner mirrors. Here the term spatial extent refers to the width of each streak to avoid confusion with the term field of view, usually reserved for spatial images. A single-axis large form factor mirror or a modification of the optical train could increase the spatial extent by a factor of up to 2.5 for the camera sensor that was used. System timing may need to be adjusted to account for changes in mirror inertia for larger galvo-mirrors [33]. While the current setup is limited to producing 2D kymograms, push broom raster scanning could be added to produce image stacks by translating either the mechanical slit or the sample for repeatable events [34].

While temporal resolution is governed primarily by the streak rate and slit width, both parameters are physically constrained by the available NV fluorescence emission. Using a sensor with a greater NV density would exhibit increased photon emission, allowing faster streak rates. It should be noted that faster streak rates would improve temporal resolution while decreasing the sequence duration. Compensation for shorter sequence duration could be made by adopting a large area sensor or wide aspect ratio sensor with the same pixel size but more pixels spanning the streak. The collection efficiency could also be increased with a higher-NA oil immersion objective, since the high refractive index of diamond results in modest losses at the NV–air boundary [35]. The magnetic field was acquired under continuous RF and optical stimulation without active or passive magnetic shielding, and no attempt was made to optimize RF antenna coupling to the NV.

This design has many potential applications where transient magnetic events can be isolated to a single spatial axis. Recent advances in NV sensors have resulted in sensitivities as low as 15 $\mathrm{pT}/\sqrt{\mathrm{Hz}}$, which allows action potentials to be measured in living organisms [10]. There is considerable interest in determining the signal contributions that different neural regions have on the overall signal, e.g., axonal segments, axon hillock, and nodes of Ranvier [36]. As of yet, transient behavior from propagating signals has not been captured because action potential durations are of the order of milliseconds and sensitivity requirements are quite restrictive [19]. By orienting neurons with respect to the slit, the proposed optical streaking method may be able to solve the temporal resolution problem, moving us closer to capturing action potential propagation free from interference caused by fluorescent dyes. Streaked magnetic field imaging could also be used to evaluate high-speed signals in transmission lines designed on PCBs [21].

While NV magnetometry is a spin projection limited technique, sensitivity is heavily influenced by photon and technical noise sources, e.g., laser intensity, temperature, and mechanical vibrations. Pulse NV interrogation protocols, such as Hahn echo or dynamic decoupling, can be implemented for higher sensitivity for narrow bandwidth AC magnetic fields [2,37]. Such techniques can readily be combined with optical streaking systems to greatly improve magnetic sensitivity by introducing a static or time dependent field to average environmental interactions to zero [38]. Aside from dynamic decoupling, common mode rejection (CMR) strategies can also be used to differentially isolate signals from background fluorescence [20,39].

While this work focuses entirely on magnetic field imaging, optical streaking could potentially be applied to localization and monitoring of active biological processes such as ATPase activity [40], measurement of fast changing electric fields [41,42], dynamic relaxometry [43–45], and rapid pressure changes [46]. This technique could also be applied to a wide range of quantum sensors and applications beyond magnetic field imaging. Several other color centers exist including silicon vacancies [47], silicon carbide [48], optically addressable molecular spins [49], and upconversion particles [50,51].

This technique was primarily motivated by its capability to be readily extended to full 3D video acquisition by utilizing compressed sensing techniques with potential frame rates of 1.5 Mfps [52]. A translating magnetized needle tip was chosen because it is analogous to video of light pulse propagation seen in compressed ultrafast photography (CUP) [22]. By introducing a pseudo-random spatial mask in place of the mechanical slit, this system should be able to leverage numerical reconstruction techniques to produce single-shot magnetic field videos. Using knowledge of the optical streaking forward model and the addition of a random spatial mask, compressed 3D information can be recovered using inverse reconstruction algorithms [53,54].

NV diamonds also exhibit an all-optical longitudinal T1 relaxation that can detect the presence of paramagnetic species via the associated change in relaxation rate [43,44,55]. With submicrosecond frame rates reported by Liu *et al.*, it could be possible to acquire changes in fluorescence during T1 relaxation, since relaxation rates in air can exceed 1 ms [52].

4. CONCLUSION

We have demonstrated an optical streaking NV magnetometer capable of capturing magnetic fields with micro-scale spatial extent and ~400 μs temporal resolution. In validating this system, we observed sensitivity to 40 Hz sinusoidal magnetic fields down to 10 μT and captured the spatial transit of an acid etched electromagnetic needle with an applied 40 Hz magnetic field at streak rates of 110 μm/ms at the camera sensor. We propose that this system has the potential to capture dynamic magnetic field events that can be isolated to a single spatial axis including action potential propagation as well as transient transmission line signaling. Future work will attempt to produce high-speed dynamic magnetic field video through compressed optical streaking strategies.

Funding. National Science Foundation (CMMI-1826078); Grantová Agentura České Republiky (GA20-28980S); Cancer Prevention and Research Institute of Texas (RP180588); NSF Graduate Research Fellowship (279451); National Institutes of Health (1R01GM127696, 1R21CA269099, 1R21GM142107); Army Medical Research (W81XWH2010777); Air Force Office of Scientific Research (17RHCOR483, 20RHCOR051, FA9550-15-1-0517, FA9550-20-1-0366, FA9550-20-1-0367); U.S. Air Force (FA8650-19-C-6024).

Acknowledgment. The authors thank Allen Kiester and Gary Noojin for their helpful advice and assistance with equipment. Thank you for all your support. Vladislav V. Yakovlev

acknowledges the support from the NSF, AFOSR, DOD Army Medical Research, NIH, and CPRIT. Mark A. Keppler was supported by an NSF Graduate Research Fellowship. Work contributed by SAIC was performed under the United States Air Force. Joel N. Bixler received funding from AFOSR. Miloš Nesládek was funded by the Grant Agency of the Czech Republic.

Disclosures. The authors declare no conflicts of interest.

Data Availability. Data underlying the results presented in this paper are not publicly available at this time but may be obtained from the authors upon reasonable request.

REFERENCES

1. G. Davies and M. F. Hamer, "Optical studies of the 1.945 eV vibronic band in diamond," Proc. R. Soc. London A **348**, 285–298 (1976).
2. J. F. Barry, J. M. Schloss, E. Bauch, M. J. Turner, C. A. Hart, and L. M. Pham, "Sensitivity optimization for NV-diamond magnetometry," Rev. Mod. Phys. **92**, 015004 (2020).
3. S. Hernández-Gómez and N. Fabbri, "Quantum control for nanoscale spectroscopy with diamond nitrogen-vacancy centers: a short review," Front. Phys. **8**, 610868 (2021).
4. T. Zhang, G. Pramanik, K. Zhang, M. Gulka, L. Wang, J. Jing, F. Xu, Z. Li, Q. Wei, P. Cigler, and Z. Chu, "Toward quantitative bio-sensing with nitrogen–vacancy center in diamond," ACS Sens. **6**, 2077–2107 (2021).
5. Y. Wu, F. Jelezko, M. B. Plenio, and T. Weil, "Diamond quantum devices in biology," Angew. Chem. **55**, 6586–6598 (2016).
6. R. Schirhagl, K. Chang, M. Loretz, and C. L. Degen, "Nitrogen-vacancy centers in diamond: nanoscale sensors for physics and biology," Annu. Rev. Phys. Chem. **65**, 83–105 (2014).
7. L. M. Pham, D. Le Sage, P. L. Stanwix, T. K. Yeung, D. Glenn, A. Trifonov, P. Cappellaro, P. R. Hemmer, M. D. Lukin, H. Park, A. Yacoby, and R. L. Walsworth, "Magnetic field imaging with nitrogen-vacancy ensembles," New J. Phys. **13**, 045021 (2011).
8. J.-C. Jaskula, E. Bauch, S. Arroyo-Camejo, M. D. Lukin, S. W. Hell, A. S. Trifonov, and R. L. Walsworth, "Superresolution optical magnetic imaging and spectroscopy using individual electronic spins in diamond," Opt. Express **25**, 11048–11064 (2017).
9. J. M. Schloss, J. F. Barry, M. J. Turner, and R. L. Walsworth, "Simultaneous broadband vector magnetometry using solid-state spins," Phys. Rev. Appl. **10**, 034044 (2018).
10. J. F. Barry, M. J. Turner, J. M. Schloss, D. R. Glenn, Y. Song, M. D. Lukin, H. Park, and R. L. Walsworth, "Optical magnetic detection of single-neuron action potentials using quantum defects in diamond," Proc. Natl. Acad. Sci. USA **113**, 14133–14138 (2016).
11. D. Le Sage, K. Arai, D. R. Glenn, S. J. Devience, L. M. Pham, L. Rahn-Lee, M. D. Lukin, A. Yacoby, A. Komeili, and R. L. Walsworth, "Optical magnetic imaging of living cells," Nature **496**, 486–489 (2013).
12. N. Mohan, C. S. Chen, H. H. Hsieh, Y. C. Wu, and H. C. Chang, "*In vivo* imaging and toxicity assessments of fluorescent nanodiamonds in caenorhabditis elegans," Nano Lett. **10**, 3692–3699 (2010).
13. G. Kucsko, P. C. Maurer, N. Y. Yao, M. Kubo, H. J. Noh, P. K. Lo, H. Park, and M. D. Lukin, "Nanometre-scale thermometry in a living cell," Nature **500**, 54–58 (2013).
14. M. Fujiwara, S. Sun, A. Dohms, Y. Nishimura, K. Suto, Y. Takezawa, K. Oshimi, L. Zhao, N. Sadzak, Y. Umehara, Y. Teki, N. Komatsu, O. Benson, Y. Shikano, and E. Kage-Nakadai, "Real-time nanodiamond thermometry probing *in vivo* thermogenic responses," Sci. Adv. **6**, eaba9636 (2020).
15. C. A. Hart, J. M. Schloss, M. J. Turner, P. J. Scheidegger, E. Bauch, and R. L. Walsworth, "N–V-diamond magnetic microscopy using a double quantum 4-Ramsey protocol," Phys. Rev. Appl. **15**, 044020 (2021).
16. J. J. Davies, "Optically-detected magnetic resonance and its applications," Contemp. Phys. **17**, 275–294 (1976).
17. A. M. Wojciechowski, M. Karadas, A. Huck, C. Osterkamp, S. Jankuhn, J. Meijer, F. Jelezko, and U. L. Andersen, "Contributed review: camera-limits for wide-field magnetic resonance imaging with a nitrogen-vacancy spin sensor," Rev. Sci. Instrum. **89**, 031501 (2018).
18. Hamamatsu, "How fast can I image?" https://camera.hamamatsu.com/jp/en/technical_guides/dissecting_camera/dissecting_camera03/index.html.
19. J. Malmivuo and R. Plonsey, *Bioelectromagnetism Principles and Applications of Bioelectric and Biomagnetic Fields* (Oxford University, 1995), Vol. **15**.
20. J. L. Webb, L. Troise, N. W. Hansen, J. Achard, O. Brinza, R. Staacke, M. Kieschnick, J. Meijer, J. F. Perrier, K. Berg-Sørensen, A. Huck, and U. L. Andersen, "Optimization of a diamond nitrogen vacancy centre magnetometer for sensing of biological signals," Front. Phys. **8**, 430 (2020).
21. K. Mizuno, H. Ishiwata, Y. Masuyama, T. Iwasaki, and M. Hatano, "Simultaneous wide-field imaging of phase and magnitude of AC magnetic signal using diamond quantum magnetometry," Sci. Rep. **10**, 11611 (2020).
22. L. Gao, J. Liang, C. Li, and L. V. Wang, "Single-shot compressed ultrafast photography at one hundred billion frames per second," Nature **516**, 74–77 (2014).
23. V. M. Acosta, A. Jarmola, E. Bauch, and D. Budker, "Optical properties of the nitrogen-vacancy singlet levels in diamond," Phys. Rev. B **82**, 201202 (2010).
24. D. R. Glenn, R. R. Fu, P. Kehayias, D. Le Sage, E. A. Lima, B. P. Weiss, and R. L. Walsworth, "Micrometer-scale magnetic imaging of geological samples using a quantum diamond microscope," Geochem. Geophys. Geosyst. **18**, 3254–3267 (2017).
25. B. D. Matthews, D. A. LaVan, D. R. Overby, J. Karavitis, and D. E. Ingber, "Electromagnetic needles with submicron pole tip radii for nanomanipulation of biomolecules and living cells," Appl. Phys. Lett. **85**, 2968–2970 (2004).
26. "Magnetic field calculator for coil," https://www.accelinstruments.com/Magnetic/Magnetic-field-calculator.html.
27. A. Kuwahata, T. Kitaizumi, K. Saichi, T. Sato, R. Igarashi, T. Ohshima, Y. Masuyama, T. Iwasaki, M. Hatano, F. Jelezko, M. Kusakabe, T. Yatsui, and M. Sekino, "Magnetometer with nitrogen-vacancy center in a bulk diamond for detecting magnetic nanoparticles in biomedical applications," Sci. Rep. **10**, 2483 (2020).
28. M. Mrózek, A. M. Wojciechowski, and W. Gawlik, "Characterization of strong NV—gradient in the e-beam irradiated diamond sample," Diam. Relat. Mater. **120**, 108689 (2021).
29. R. Rubinas, V. V. Vorobyov, V. V. Soshenko, S. V. Bolshedvorskii, V. N. Sorokin, A. N. Smolyaninov, V. G. Vins, A. P. Yelisseyev, and A. V. Akimov, "Spin properties of NV centers in high-pressure, high-temperature grown diamond," J. Phys. Commun. **2**, 115003 (2018).
30. T. Mittiga, S. Hsieh, C. Zu, B. Kobrin, F. Machado, P. Bhattacharyya, N. Z. Rui, A. Jarmola, S. Choi, D. Budker, and N. Y. Yao, "Imaging the local charge environment of nitrogen-vacancy centers in diamond," Phys. Rev. Lett. **121**, 246402 (2018).
31. F. Alghannam and P. Hemmer, "Engineering of shallow layers of nitrogen vacancy colour centres in diamond using plasma immersion ion implantation," Sci. Rep. **9**, 5870 (2019).
32. Z. Ma, S. Zhang, Y. Fu, H. Yuan, Y. Shi, J. Gao, L. Qin, J. Tang, J. Liu, and Y. Li, "Magnetometry for precision measurement using frequency-modulation microwave combined efficient photon-collection technique on an ensemble of nitrogen-vacancy centers in diamond," Opt. Express **26**, 382–390 (2018).
33. M. Pothen, K. Winands, and F. Klocke, "Compensation of scanner based inertia for laser structuring processes," J. Laser Appl. **29**, 012017 (2017).
34. S. Ortega, R. Guerra, M. DIaz, H. Fabelo, S. Lopez, G. M. Callico, and R. Sarmiento, "Hyperspectral push-broom microscope development and characterization," IEEE Access **7**, 122473 (2019).
35. D. A. Hopper, H. J. Shulevitz, and L. C. Bassett, "Spin readout techniques of the nitrogen-vacancy center in diamond," Micromachines **9**, 437 (2018).

36. M. Parashar, K. Saha, and S. Bandyopadhyay, "Axon hillock currents enable single-neuron-resolved 3D reconstruction using diamond nitrogen-vacancy magnetometry," Commun. Phys. **3**, 174 (2020).
37. D. Suter and F. Jelezko, "Single-spin magnetic resonance in the nitrogen-vacancy center of diamond," Prog. Nucl. Magn. Reson. Spectrosc. **98–99**, 50–62 (2017).
38. D. Suter and G. A. Álvarez, "Colloquium: protecting quantum information against environmental noise," Rev. Mod. Phys. **88**, 041001 (2016).
39. M. Mrózek, D. Rudnicki, P. Kehayias, A. Jarmola, D. Budker, and W. Gawlik, "Longitudinal spin relaxation in nitrogen-vacancy ensembles in diamond," EPJ Quantum Technol. **2**, 22 (2015).
40. L. P. McGuinness, Y. Yan, A. Stacey, D. A. Simpson, L. T. Hall, D. Maclaurin, S. Prawer, P. Mulvaney, J. Wrachtrup, F. Caruso, R. E. Scholten, and L. C. L. Hollenberg, "Quantum measurement and orientation tracking of fluorescent nanodiamonds inside living cells," Nat. Nanotechnol. **6**, 358–363 (2011).
41. M. Block, B. Kobrin, A. Jarmola, S. Hsieh, C. Zu, N. L. Figueroa, V. M. Acosta, J. Minguzzi, J. R. Maze, D. Budker, and N. Y. Yao, "Optically enhanced electric field sensing using nitrogen-vacancy ensembles," Phys. Rev. Appl. **16**, 024024 (2021).
42. F. Dolde, H. Fedder, M. W. Doherty, T. Nöbauer, F. Rempp, G. Balasubramanian, T. Wolf, F. Reinhard, L. C. L. Hollenberg, F. Jelezko, and J. Wrachtrup, "Electric-field sensing using single diamond spins," Nat. Phys. **7**, 459–463 (2011).
43. F. Gorrini, R. Giri, C. E. Avalos, S. Tambalo, S. Mannucci, L. Basso, N. Bazzanella, C. Dorigoni, M. Cazzanelli, P. Marzola, A. Miotello, and A. Bifone, "Fast and sensitive detection of paramagnetic species using coupled charge and spin dynamics in strongly fluorescent nanodiamonds," ACS Appl. Mater. Interfaces **11**, 24412–24422 (2019).
44. S. Steinert, F. Ziem, L. T. Hall, A. Zappe, M. Schweikert, N. Götz, A. Aird, G. Balasubramanian, L. Hollenberg, and J. Wrachtrup, "Magnetic spin imaging under ambient conditions with sub-cellular resolution," Nat. Commun. **4**, 1607 (2013).
45. F. Perona Martínez, A. C. Nusantara, M. Chipaux, S. K. Padamati, and R. Schirhagl, "Nanodiamond relaxometry-based detection of free-radical species when produced in chemical reactions in biologically relevant conditions," ACS Sens. **5**, 3862–3869 (2020).
46. M. W. Doherty, V. V. Struzhkin, D. A. Simpson, L. P. McGuinness, Y. Meng, A. Stacey, T. J. Karle, R. J. Hemley, N. B. Manson, L. C. L. Hollenberg, and S. Prawer, "Electronic properties and metrology applications of the diamond NV-center under pressure," Phys. Rev. Lett. **112**, 047601 (2014).
47. S. Lagomarsino, A. M. Flatae, H. Kambalathmana, F. Sledz, L. Hunold, N. Soltani, P. Reuschel, S. Sciortino, N. Gelli, M. Massi, C. Czelusniak, L. Giuntini, and M. Agio, "Creation of silicon-vacancy color centers in diamond by ion implantation," Front. Phys. **8**, 626 (2021).
48. S. Castelletto and A. Boretti, "Silicon carbide color centers for quantum applications," J. Phys. Photon. **2**, 022001 (2020).
49. S. L. Bayliss, D. W. Laorenza, P. J. Mintun, B. D. Kovos, D. E. Freedman, and D. D. Awschalom, "Optically addressable molecular spins for quantum information processing," Science **370**, 1309–1312 (2020).
50. F. Vetrone, R. Naccache, A. Zamarrón, A. J. De La Fuente, F. Sanz-Rodríguez, L. M. Maestro, E. M. Rodriguez, D. Jaque, J. G. Sole, and J. A. Capobianco, "Temperature sensing using fluorescent nanothermometers," ACS Nano **4**, 3254–3258 (2010).
51. X. Liu, A. Skripka, Y. Lai, C. Jiang, J. Liu, F. Vetrone, and J. Liang, "Fast wide-field upconversion luminescence lifetime thermometry enabled by single-shot compressed ultrahigh-speed imaging," Nat. Commun. **12**, 6401 (2021).
52. X. Liu, J. Liu, C. Jiang, F. Vetrone, and J. Liang, "Single-shot compressed optical-streaking ultra-high-speed photography," Opt. Lett. **44**, 1387–1390 (2019).
53. E. J. Candès, J. Romberg, and T. Tao, "Robust uncertainty principles: exact signal reconstruction from highly incomplete frequency information," IEEE Trans. Inf. Theory **52**, 489–509 (2006).
54. S. Voronin and C. Zaroli, "Survey of computational methods for inverse problems," in *Recent Trends in Computational Science and Engineering* (InTech, 2018), Vol. **3**.
55. V. Radu, J. C. Price, S. J. Levett, K. K. Narayanasamy, T. D. Bateman-Price, P. B. Wilson, and M. L. Mather, "Dynamic quantum sensing of paramagnetic species using nitrogen-vacancy centers in diamond," ACS Sens. **5**, 703–710 (2020).